

# Reconstruction and Visualization of Fiber and Laminar Structure in the Normal Human Heart from Ex Vivo Diffusion Tensor Magnetic Resonance Imaging (DTMRI) Data

*Damien Rohmer, MS, Arkadiusz Sitek, PhD, and Grant T. Gullberg, PhD*

**Objective:** The human heart is composed of a helical network of muscle fibers organized to form sheets that are separated by cleavage planes responsible for the orthotropic mechanical properties of cardiac muscle. The purpose of this study is the reconstruction and visualization of these structures in 3 dimensions.

**Methods:** Anisotropic least square filtering followed by fiber and sheet tracking techniques were applied to diffusion tensor magnetic resonance imaging data of the excised human heart. Fibers were reconstructed using the first eigenvectors of the diffusion tensors. The sheets were reconstructed using the second and third eigenvectors and visualized as surfaces.

**Results:** The fibers are shown to lie in sheets that have transmural structure, which correspond to histologic studies published in the literature. Quantitative measurements show that the sheets as oppose to the fibers are organized into laminar orientations without dominant populations.

**Conclusions:** A visualization algorithm was developed to demonstrate the complex 3-dimensional orientation of the fibers and sheets in human myocardium.

**Key Words:** cardiac imaging, diffusion tensor MRI, fiber tracking, laminar structure

*(Invest Radiol 2007;42: 777–789)*

Received July 21, 2006, and accepted for publication, after revision, May 21, 2007.

From the Life Sciences Division, Ernest Orlando Lawrence Berkeley National Laboratory, Berkeley, California.

Arkadiusz Sitek, PhD, is currently at the Department of Radiology, Harvard Medical School, Brigham and Women's Hospital, Boston, Massachusetts.

Damien Rohmer is currently at Laboratoire Jean Kuntzmann, Institut National Polytechnique de Grenoble, Grenoble, France.

Supported by the Director, Office of Science, Office of Biological and Environmental Research, Medical Science Division of the US Department of Energy under Contract No. DE-AC03-76SF00098 and in part by Public Health Service grant number R01EB000121 awarded by the National Institute of Biomedical Imaging and Bioengineering, Department of Health and Human Services.

Reprints: Grant T. Gullberg, PhD, Lawrence Berkeley Laboratory, 1 Cyclotron Road, MS55R0121, Berkeley, CA 94720. E-mail: GTGullberg@lbl.gov.

Copyright © 2007 by Lippincott Williams & Wilkins

ISSN: 0020-9996/07/4211-0777

The human heart is composed of a helical network of muscle fibers<sup>1,2</sup> organized to form sheets that are separated by a complex structure of cleavage planes.<sup>2</sup> Understanding the 3-dimensional (3D) configuration of the fiber and sheet structure is of utmost importance for modeling the mechanical<sup>2–4</sup> and electrical properties<sup>5</sup> of the heart; and changes in this configuration may be of significant importance to understand the remodeling after myocardial infarction.<sup>6</sup> The visual comprehension of this anatomic structure is helpful to better understand the implications of the structure as to its relationship to the electrical, mechanical, and biochemical properties of the heart. A comprehensive way to visualize these fibers is the use of 3D paths throughout the ventricle where the sheets are well represented by their cleavage planes. It is known that the principle eigenvector of the diffusion tensor obtained from diffusion tensor magnetic resonance imaging (DTMRI) can be used to determine the fiber direction. However, the second and third eigenvectors of the tensor are also of interest and provide important information associated with the sheet geometry.<sup>7–11</sup>

The left ventricle is organized in a collection of 3D muscle fibers composed of myocytes (muscle cells) where each are 80–100  $\mu\text{m}$  in length and have a cylindrical shape with a radius of 5–10  $\mu\text{m}$ .<sup>4,12</sup> To preserve the tissue architecture, especially during large deformations of contractile motion, cardiac fibers are embedded in an extracellular matrix called endomysium that consists of collagen where the type III collagen<sup>6,13</sup> (highly deformable) has the highest proportion. Histologic studies have shown that the orientation of the fiber angles vary continuously from approximately  $+60^\circ$  to  $-60^\circ$  across the wall,<sup>1</sup> where from the apex to the base the fibers are a left-handed spiral from the epicardium to the midwall, have a planar circular geometry in the midwall, and are a right-handed spiral from the midwall to the endocardium.

The fibers in the heart form another 3D structure due to the alignment of the fibers in sheets.<sup>4,12,14,15</sup> Histologic studies show that the fibers are grouped in a volume of 3–4 cells thick within a laminar structure oriented transversally to the heart-wall.<sup>2</sup> This laminar structure is bounded by cleavage planes that are responsible for some of the important mechanical properties of the cardiac muscle.<sup>2,16</sup> These surfaces exhibit an orientation, which varies spatially showing a com-

plex structure inside the heart.<sup>17</sup> The laminar structure can be roughly seen as bounded by twisted surfaces going across the wall and stacked from apex to base.<sup>14</sup> The sheets are physically separated by a coiled bundle of collagen fibers called perimysium.<sup>4,12,18</sup> This collagen consists mainly of type I (72%) (high tensile strength). The local geometry of the cleavage plane is characterized by the normal of the sheet at each position. Histologic measurements have shown that this angle varies with the position across the wall (from +45° to -80°) and the distribution changes from the apical region (roughly convex variation across the wall) to the basal region (concave variation).<sup>17,19</sup>

The diffusion tensor can be decomposed into eigenvalues and eigenvectors where the eigenvalues are sorted in decreasing order. Histology measurements have already validated the DTMRI measurement of the fiber direction with high precision.<sup>20,21</sup> Based on the assumption that the water contained inside and outside the heart fiber cannot move freely, but is constrained to move in the direction of the fiber itself,<sup>22,23</sup> it is confirmed that the first eigenvector corresponding to the largest direction of the diffusion is aligned with the direction of the fiber. The information of the fiber angle for each voxel can be sufficient for mechanical studies of the motion of the heart,<sup>24,25</sup> however, the anatomic structure of the fiber is not apparent unless the path of the fibers is followed to produce a 3D visualization of its structure. The fiber tracking method<sup>26</sup> helps the perception of this architecture by reconstructing the path followed by the fibers. With the visual information of the fiber linkage, a better comprehension of physical relationships between endocardium and epicardium and right and left ventricle is facilitated.<sup>27</sup> In addition, when a change occurs after cardiac remodeling<sup>6,28-30</sup> due to infarct or surgery,<sup>31</sup> the visualization of the fiber path may be helpful for understanding the induced structural alterations.

The fiber tracking method is widely used in the brain to follow the white matter axons; however, some differences in the heart have to be taken into account. The white matter shows large differences of eigenvalues between the largest eigenvalue and the other 2 eigenvalues; and large variations of the ratio between these eigenvalues are present inside the brain.<sup>32</sup> For the heart, however, the ratio between the first and the second eigenvalue is roughly constant between 1.5 and 2. Therefore, techniques based on the change of anisotropy are not appropriate for cardiac fiber tracking. Additionally, in the heart, the fibers are organized in layers (sheets) separated physically by cleavage planes. This makes the diffusion smaller in the normal direction of the cleavage planes than diffusion inside the cleavage planes. The cleavage plane acts like a barrier to the diffusion. Because of that, the second eigenvector of the diffusion tensor is assumed to be positioned inside the sheet, and the third (the smallest one) is assumed locally to be normal to the sheet. These assumptions have been recently studied and a good correlation between histologic measurements and analysis of DTMRI data for both fiber and sheet structure has been shown.<sup>10,20,33</sup> The information of the sheet angle given at every position of the heart is of major interest for the mechanical modeling of the orthotropic distribution of strain and stress,<sup>12,20</sup> but

the perception of the real anatomic geometry is facilitated by the 3D visualization of the surfaces within the heart wall. This visualization is even more important for the sheet structure as the perception of a surface is more complex than a curve.

The visualization of the fibers in the heart is still a new field of research. Only a few articles presenting graphical visualization of the heart fiber structure have been published for canine,<sup>8,34,35</sup> mouse,<sup>36</sup> or porcine<sup>37</sup> hearts. Some results showing the sheet orientation in canine heart has also been presented.<sup>35</sup> In the present article, the representation is performed on a normal excised human heart. To the best of our knowledge, this is the first article obtaining the 3D visualization of the sheet structure from DTMRI data.

In the present article, first a method for anisotropic filtering is presented to regularize the available DTMRI data of a human heart. Then, a fiber tracking algorithm and an algorithm for the reconstruction of the sheet structure are described. Based on the expected geometry of the sheet, the algorithm uses the 2 smallest eigenvectors of the tensor to reconstruct the sheet as a surface. Finally, a comprehensive visualization of fiber paths and sheet surfaces are presented using a high quality ray-tracer.

## METHODS

### DTMRI Human Heart Data

The data were acquired in the Laboratory of Dr. Elliot McVeigh at NIH working in collaboration with Drs. Rai Winslow and Patrick Helm at Johns Hopkins University. The data were acquired using a normal excised human heart and was made available for downloading on the internet (<http://www.ccbm.jhu.edu/research/DTMRIDS.php>). The heart was placed in an acrylic container filled with Fomblin (Ausimon, Thorofare, NJ), a perfluoropolyether having a low dielectric effect and low MR signal to increase tissue-fluid contrast. This setup also eliminated unwanted susceptibility artifacts near the boundaries of the heart. Images were acquired with a 4-element phased array coil on a 1.5 T GE CV/I MRI Scanner (GE Medical System, Wausheka, WI) using an enhanced gradient system with 40 mT/m maximum gradient amplitude and a 150 T/m/s slew rate. The acquisition was performed similar to that performed in canine hearts<sup>9</sup> using a diffusion-weighted 3D fast spin-echo pulse sequence. The field of view was 10 cm. Gradient pulses were 20 milliseconds in duration with trapezoidal shape. The TR was set to 500 milliseconds with 2 averages. The diffusion encoding was produced using a pair of gradient pulses placed symmetrically around the first 180° RF pulse. Nineteen diffusion-weighted scans and 2 scans without diffusion gradients were performed with a *b* value of 1500 s/mm<sup>2</sup>. The acquisition was performed over almost 60 hours of continuous imaging time.

The data set was arranged in a 256 × 256 × 134 array where each voxel in the array consisted of the 3 eigenvalues and 3 eigenvectors. The size of each voxel was 429.7 μm × 429.7 μm × 1000 μm.

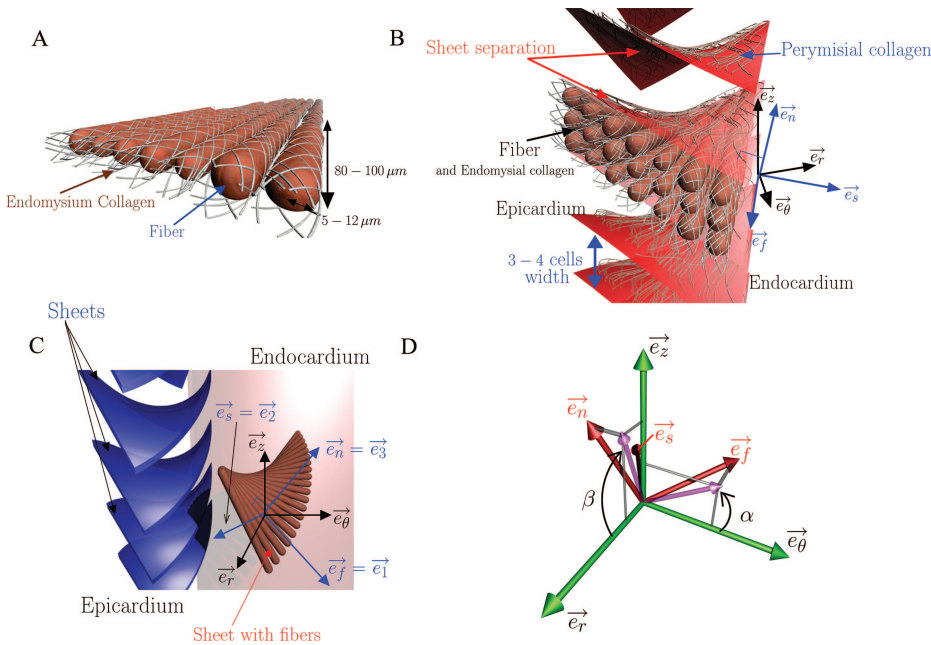


**FIGURE 1.** Representation of the fibers in the heart. A, The long oval structures correspond to the fibers. B, The laminar structure in the heart is represented with the cylindrical basis ( $\vec{e}_r, \vec{e}_\theta, \vec{e}_z$ ) and the sheet basis with the basis ( $\vec{e}_f, \vec{e}_s, \vec{e}_n$ ). C, Simplified visualization of the sheet and fiber spatial arrangement with the associated coordinate system. ( $\vec{e}_f = \vec{e}_1$ ) is the fiber direction, ( $\vec{e}_s = \vec{e}_2$ ) is the sheet direction, and  $\vec{e}_n$  is the normal to the sheet, where  $\vec{e}_1, \vec{e}_2$ , and  $\vec{e}_3$  are eigenvectors of the diffusion tensor. D, Definition of the fiber angle  $\alpha$  and sheet angle  $\beta$ .

**Mathematical Model**

The left ventricle is described with a cylindrical coordinate system with basis ( $\vec{e}_r, \vec{e}_\theta, \vec{e}_z$ ), where  $\vec{e}_r$  is the radial component orthogonal to the wall,  $\vec{e}_\theta$  the circumferential, and  $\vec{e}_z$  the axial component from apex to base. The fiber direction is denoted as  $\vec{e}_f$  and the unitary sheet normal is denoted as  $\vec{e}_n$  as seen in Figure 1B, C. The vector  $\vec{e}_s$  is chosen to lie inside the sheet so that the basis ( $\vec{e}_f, \vec{e}_s, \vec{e}_n$ ) is orthonormal.

The fiber angle  $\alpha$  is defined as the angle between the projection of  $\vec{e}_f$  onto the plane ( $\vec{e}_\theta, \vec{e}_z$ ). As defined in the article by Helm et al,<sup>9</sup> the sheet angle  $\beta$  is defined as the angle between the projection of  $\vec{e}_n$  onto the plane ( $\vec{e}_r, \vec{e}_z$ ).

The diffusion tensor  $D$  is decomposed into eigenvectors  $\vec{e}_1, \vec{e}_2$ , and  $\vec{e}_3$  with eigenvalues  $\lambda_1, \lambda_2$ , and  $\lambda_3$ , such that  $\lambda_1 \geq \lambda_2 \geq \lambda_3$ . Denoting  $R$  as the matrix of eigenvectors and  $\Lambda = \text{diag}(\lambda_1, \lambda_2, \lambda_3)$  as the diagonal matrix of eigenvalues, the diffusion tensor can be decomposed as  $D = R \Lambda R^T$ . As in our previous discussion, it is hypothesized that  $(\vec{e}_1, \vec{e}_2, \vec{e}_3) = (\vec{e}_f, \vec{e}_s, \vec{e}_n)$ .

**Fiber Tracking Algorithm**

A common way to render a continuous vector field is to use fiber tracking (streamline).<sup>34,38-40</sup> Given an initial position within the myocardium, a particle moves within the vector field described by the first eigenvector  $\vec{e}_1$  of the diffusion tensor and its trajectory is parameterized. The mathematical formulation of the fiber tracking is to find the path  $\vec{s}$  which depends on the variable  $t$  where  $\vec{s}_0$  is the initial position:

$$\begin{cases} \vec{s}'(t) = \vec{e}_1(\vec{s}(t)) \\ \vec{s}(0) = \vec{s}_0 \end{cases} \quad (1)$$

This is a first-order nonlinear ordinary differential equation. In this article, a fifth order Dormand-Prince

Runge-Kutta method<sup>41</sup> with automatic error estimation is used to solve Eq. (1).

The data provide the average of the fiber direction over a voxel, which contains roughly 4600 fibers if we assume a voxel volume of  $(429 \times 429 \times 100) \mu\text{m}^3$  with 100% packing of myocytes with a volume of  $(20 \times 20 \times 100) \mu\text{m}^3$ . We should then expect to see a smooth orientation along the heart without noise. However, noise can be noticed when computing fiber tracks directly from the DTMRI data without applying any method for smoothing. To minimize these effects, an anisotropic filtering method was used to smooth the directions of the fibers. We chose to implement the moving least squares (MLS) method,<sup>38</sup> which gives a point-to-point filter with respect to the local direction of the anisotropy. The method minimizes the following energy functional by constructing an approximate polynomial expression  $\tilde{D}$  for the tensor field  $D$  at each position  $\vec{p}$  inside the left ventricle:

$$E(\vec{p}) = \int_{\vec{p}' \in \text{heart}} G(\vec{p}' - \vec{p}) \left( \tilde{D}(\vec{p}' - \vec{p}) - D(\vec{p}') \right)^2 d\vec{p}' \quad (2)$$

The integrand includes a Gaussian weighting function  $G$ .  $\tilde{D}$  is the polynomial tensor estimated from the original tensor field  $D$ . The product of tensors is understood to be the product of each individual component.

To take into account the anisotropy,  $G$  is designed to promote the direction of the first eigenvector. Equation (2) was implemented by taking into account a Gaussian function with a standard deviation of 1 voxel in the fiber direction and 0.5 in the other 2 directions. A ratio of 2:1 was chosen recognizing the fact that the average diffusivity in the principal direction is larger than the diffusivity in the orthogonal directions. The second and

third eigenvectors, which have very close corresponding eigenvalues, were not differentiated for the purpose of filtering. The term  $G$  serves to smooth local pixels according to the tensor components of its neighbors, but the extent to which it relies on its neighbors depends on the width of the Gaussian filter in each direction. In our case, the direct neighbors (closest voxel) in the fiber direction had a weight of almost 1 and the neighbors that are located 3 voxels away from the center voxel had a weight of almost zero. The linear system given by this method was solved by Gaussian elimination and numerical integration was realized by Gaussian quadrature of order 4 in a neighborhood of 3 voxels.

Values of the tensor field were only known at discrete positions. The value of the tensor needed to be interpolated in the integration or in the regularization step to obtain the value of the vector field  $\vec{e}_f(s)$  between sampling points. The component-wise tensor interpolation was performed using trilinear interpolation. An interpolation polynomial of order 3 was chosen for  $\vec{D}$  to eliminate noise along the fiber track.

For the case of myocardial tissue fibers, the diffusion tensor is symmetric. Therefore, the sign of the eigenvector is not meaningful. Thus, to continue to move forward, a condition was needed to specify the new direction. This condition inverted the sign of the new direction if the angle between the new and old direction was greater than  $\pi/2$ .

### Sheet Tracking Algorithm

The diffusion tensor can also provide information about the laminar structure of the myocardium. For each

position in the left ventricle, a tangent plane to the sheet was found. This plane was defined by the normal vector  $\vec{e}_3 = \vec{e}_n$ . To span a sheet surface, the direction  $\vec{e}_r$  was used. Because the sheet surface is expected to cross the ventricular wall (Fig. 2), we assumed the best direction along which the plane could be defined is radially oriented across this wall. The sheet was tracked in this direction by projecting the desired direction  $\vec{e}_r$  onto the local plane defined by the fiber and sheet directions  $\vec{e}_f$  and  $\vec{e}_s$  (Fig. 3). The first spanned direction  $\vec{d}_1$  was determined by

$$\vec{d}_1 = (\vec{e}_r \cdot \vec{e}_f)\vec{e}_f + (\vec{e}_r \cdot \vec{e}_s)\vec{e}_s \tag{3}$$

The vector  $\vec{d}_1$  was used to follow the surface in this direction using a first-order Newton iteration.

To construct a 2D surface, the expansion in a perpendicular direction  $\vec{d}_2$  was performed. The vector  $\vec{d}_2$  was found by rotating the vector  $\vec{d}_1$  by a right angle around the normal of the sheet surface (Fig. 4):

$$\vec{d}_2 = (\vec{d}_1 \cdot \vec{e}_3)\vec{e}_3 - \vec{d}_1 \times \vec{e}_3 \tag{4}$$

Where  $\vec{e}_3 = \pm \vec{e}_3$  depending on the convention. The sheet was also followed along the direction  $\vec{d}_2$  using a first-order Newton iteration. This algorithm built the sheet surface from any starting point within the myocardium. The data were also filtered with the same MLS method that was used for fiber tracking. For more details about the algorithm, please refer to our LBNL report.<sup>27</sup>

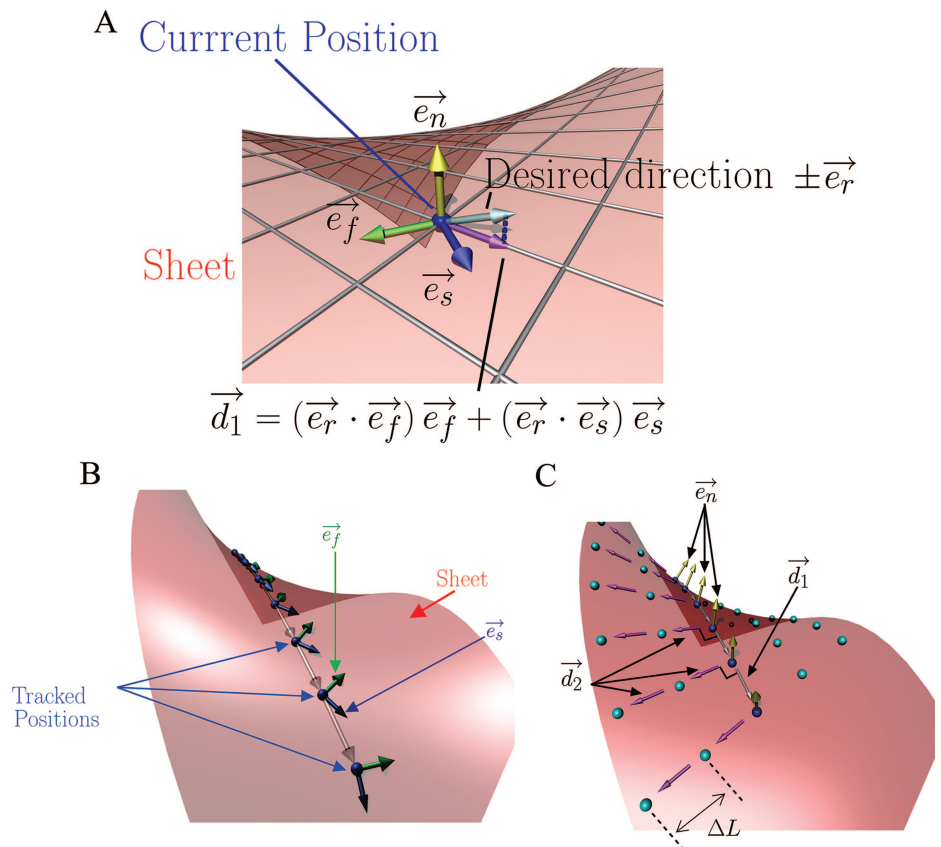


**FIGURE 2.** A, Projection of the desired radial direction  $\vec{e}_r$  onto the sheet surface defined by the normal  $\vec{e}_n$ . Vector  $\vec{e}_f$  is the fiber direction and  $\vec{e}_s$  is the sheet direction.  $\vec{d}_1$  is the projection of  $\vec{e}_r$  onto the plane spanned by the vectors  $\vec{e}_f$  and  $\vec{e}_s$ . B, Reconstruction in the radial direction (first step used for the construction of the sheet). At each position (blue spheres), the fiber direction  $\vec{e}_f$  and the sheet direction  $\vec{e}_s$  are determined from the data. The projected desired radial directions  $\vec{d}_1$  are in transparent white. C, Reconstruction in the circumferential direction. The yellow vectors  $\vec{e}_n$  are normal to the surface and the perpendicular directions  $\vec{d}_2$  (shown in magenta) are the reconstructed circumferential directions.

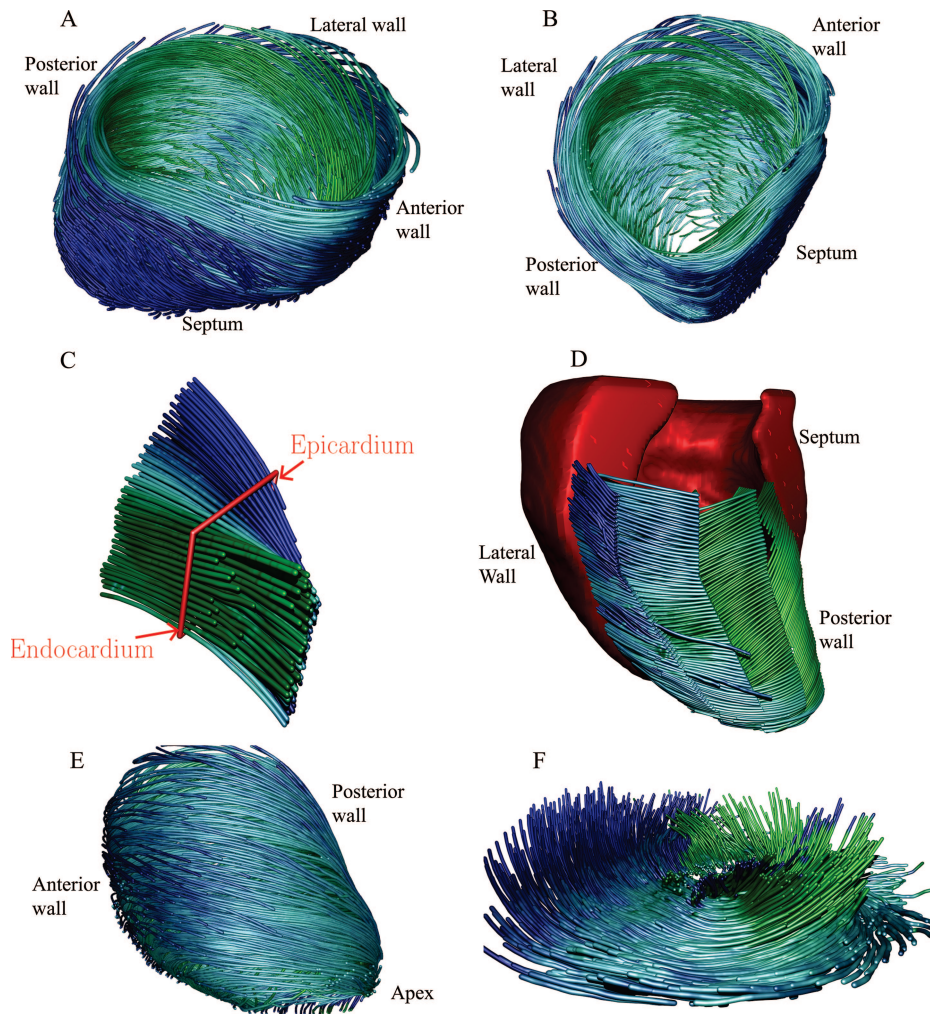


**FIGURE 3.** Visualization of the fiber structure of the left ventricle. A, The visualization was created by using a cylindrical mesh of 1000 seed points throughout the entire volume. Left-handed to right-handed rotation of the fibers going from the epicardium to endocardium can be seen. The nearest wall is the septum. B, The heart is displayed with the posterior wall on the bottom. C, Short section of the left ventricle which illustrates the smooth variation of the fiber angle and its sign inversion across the wall from epicardium to endocardium. D, Orientation of the fibers by sections in the anterior wall from septal to lateral wall. For each section, the fibers are plotted closer to the endocardium. The smooth change of direction can be seen while the fiber bundle wraps around the endocardium. E, Helical visualization of the fibers from apex to base. F, Fiber tracks close to the apex. The twist around the apex can be appreciated. It is worth noticing the smooth continuity of some bundles of fibers going down from the endocardium (green), pass the midwall (in light blue) and going up again (dark blue). The large variations between green and blue in the middle of the apex are due to the fast change from left-handed to right-handed rotation. In the center, the comparison between left-handed and right-handed rotation is not accurate as the fibers become more aligned with the central axis of the left ventricle.

### Visualization of the Fiber and Sheet Tracking Results

The fibers were represented as thin tube-like surfaces with a radius of roughly  $400 \mu\text{m}$ . Sheets defined as a set of parameterized points were triangulated creating meshed surfaces. The tubes and triangulated surfaces were displayed using the open source ray tracer Persistence of Vision Raytracer (POV-Ray) (<http://www.povray.org>). We chose the software to obtain a high quality rendering with

lighting and shadowing giving better quality images than the triangle-based render. The scene description in a POV-Ray script language was generated by fiber and sheet tracking routines.

### Quantitative Measurement of Fiber and Sheet Angles

The quantitative measurements of the fiber and sheet angles were performed by averaging the values of the

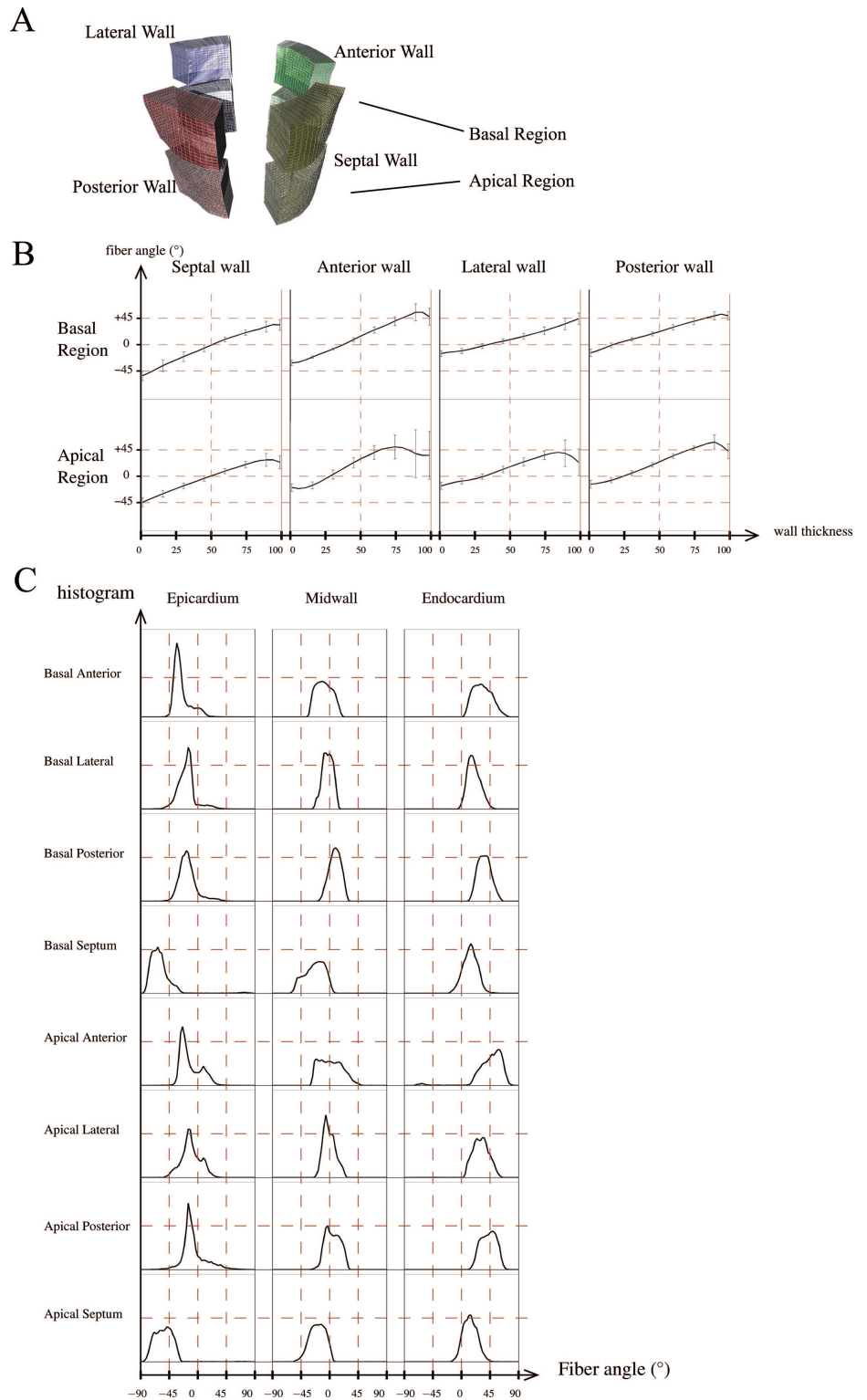


**FIGURE 4.** Quantitative distribution of the fiber angles  $\alpha$ . **A**, Regions of the ventricle that are used for sampling the fiber angle. **B**, Plot of the fiber angle from epicardium to endocardium in percent of the wall thickness. The values correspond to the average over 1800 nodes and the error bars correspond to the standard deviation of the samples. **C**, Histograms of the fiber angles for the regions as defined in (A). Each region is separated across the wall into epicardium, midwall, and endocardium sections.

angle  $\alpha$  and  $\beta$  across the wall in 8 different regions as seen in Figure 3A. The regions were defined manually on a cylindrical model of the left ventricle. Each region was sampled from 1800 nodes across the wall. The width between the samples depended on the location in the wall

of the ventricle and was expressed in percent of the total thickness. The histograms of the fiber angle  $\alpha$  and sheet angle  $\beta$  were also plotted for the same 8 regions of the ventricle. The regions were defined similar to those defined by Helm et al.<sup>9</sup>

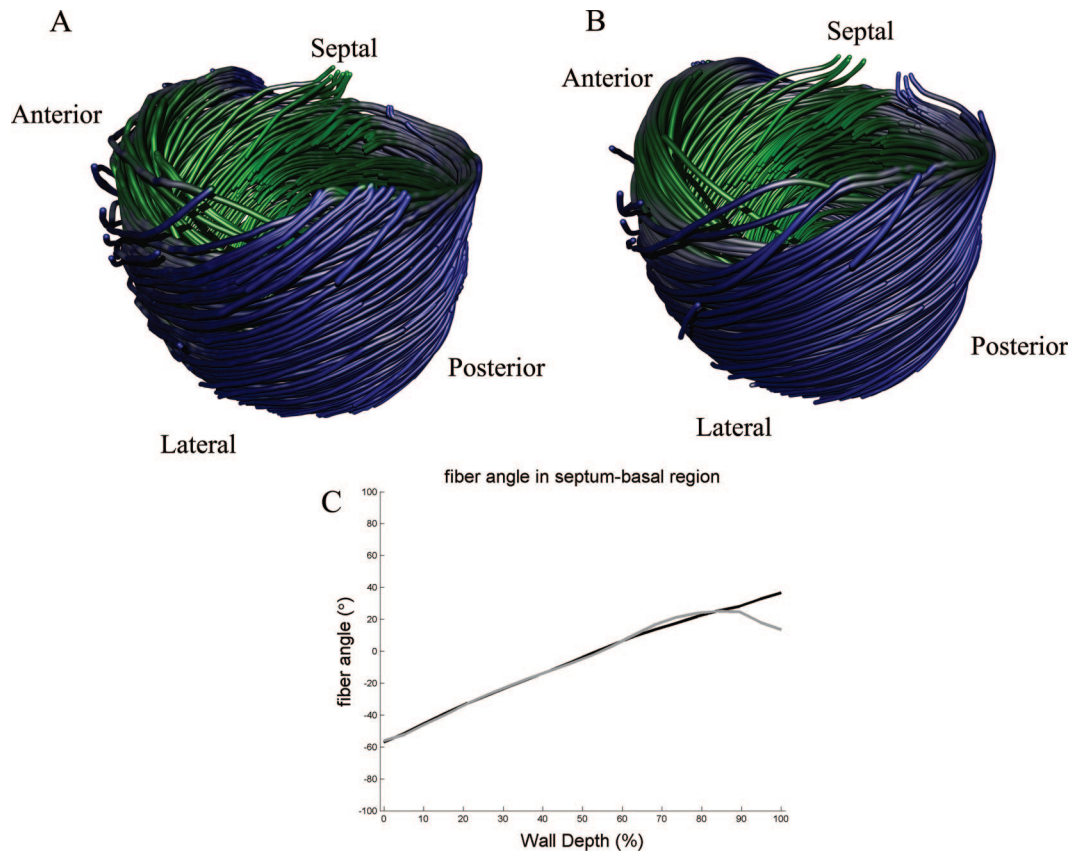


**FIGURE 5.** Comparison between unfiltered and filtered data. Comparison of the result of the fiber tracking for the entire ventricle: A, The left part represents the fiber track for the unfiltered case where some noisy oscillation can be seen in the epicardial regions, whereas B, the right part shows the result for the filtered data. The color encoding is the same as for the previous pictures. C, Comparison of the fiber angle in the filtered and unfiltered data. The black line is the fiber angle after the filtering, whereas the gray line is the fiber angle before applying the filter.

## RESULTS

Results of fiber tracking are presented in Figure 3. The visualization of the fibers in Figure 3 uses a color coding representation of the local fiber angle  $\alpha$ . Left-handed spiraling fibers are encoded with a blue color and right-handed spiraling fibers with a green color. The color intensity depends on the value of  $\alpha$ . The dark blue and dark green colors represent larger angles for the epicardium and endocardium, respectively. The light blue color in the midwall indicates fibers are located in the axial plane. On each picture the color intensity is scaled to its maximum angle. The fiber angles appear to vary smoothly across the wall. A different structure is evident in the apex of the heart where a twist of the fiber bundles is observed.

Quantitative results for the fiber angle  $\alpha$  are shown in Figure 4. In the basal region, the fiber angle increases smoothly from  $-57.07^\circ \pm 8.61^\circ$  to  $+36.50^\circ \pm 12.66^\circ$ ,  $-33.3^\circ \pm 4.87^\circ$  to  $+59.03^\circ \pm 29.64^\circ$ ,  $-16.29^\circ \pm 5.1^\circ$  to  $+47.15^\circ \pm 14.22^\circ$ , and  $-15.13^\circ \pm 6.6^\circ$  to  $+55.51^\circ \pm 7.83^\circ$  from epicardium to endocardium in the septal, anterior, lateral, and posterior regions, respectively; whereas for the apical region from  $-47.91^\circ \pm 8.36^\circ$  to  $+29.73^\circ \pm 11.79^\circ$ ,  $-22.91^\circ \pm 4.31^\circ$  to  $53.42^\circ \pm 21.96^\circ$ ,  $-17.82^\circ \pm$

$6.27^\circ$  to  $+43.38^\circ \pm 13.78^\circ$ , and  $-14.87^\circ \pm 7.15^\circ$  to  $+62.3^\circ \pm 13.14^\circ$ , respectively. The fiber angle varies linearly within the midwall but becomes more nonlinear close to the epicardial and endocardial boundaries. One thing to note is that the curves for the fiber angles strictly decrease from epicardium to endocardium. However, in some cases, a minimum is found in the endocardium or a maximum in the epicardium that are not at the extreme boundary. It is possible that the segmentation incorrectly differentiated between myocardial and non myocardial tissue of papillary and trabecular muscle. Also, the noise is greater in the endocardial and epicardial regions resulting in larger deviations and variances for the angle  $\alpha$ . The large fluctuations are especially seen in the apical region.

Our results in the 1 heart we studied showed differences to those of Helm et al<sup>9</sup> who applied DTMRI in excised canine hearts. They reported fiber angles ranging from epicardium to endocardium from  $-35.7 \pm 8.6^\circ$  to  $38 \pm 6.1^\circ$ ,  $-41.0 \pm 8.0^\circ$  to  $29.7 \pm 6.6^\circ$ , and  $-57.0 \pm 6.2^\circ$  to  $39.5 \pm 10.6^\circ$  in the anterior, lateral, and posterior regions, respectively. They found the range of helix angles larger in the posterior region than in the anterior region, which was opposite of our results.

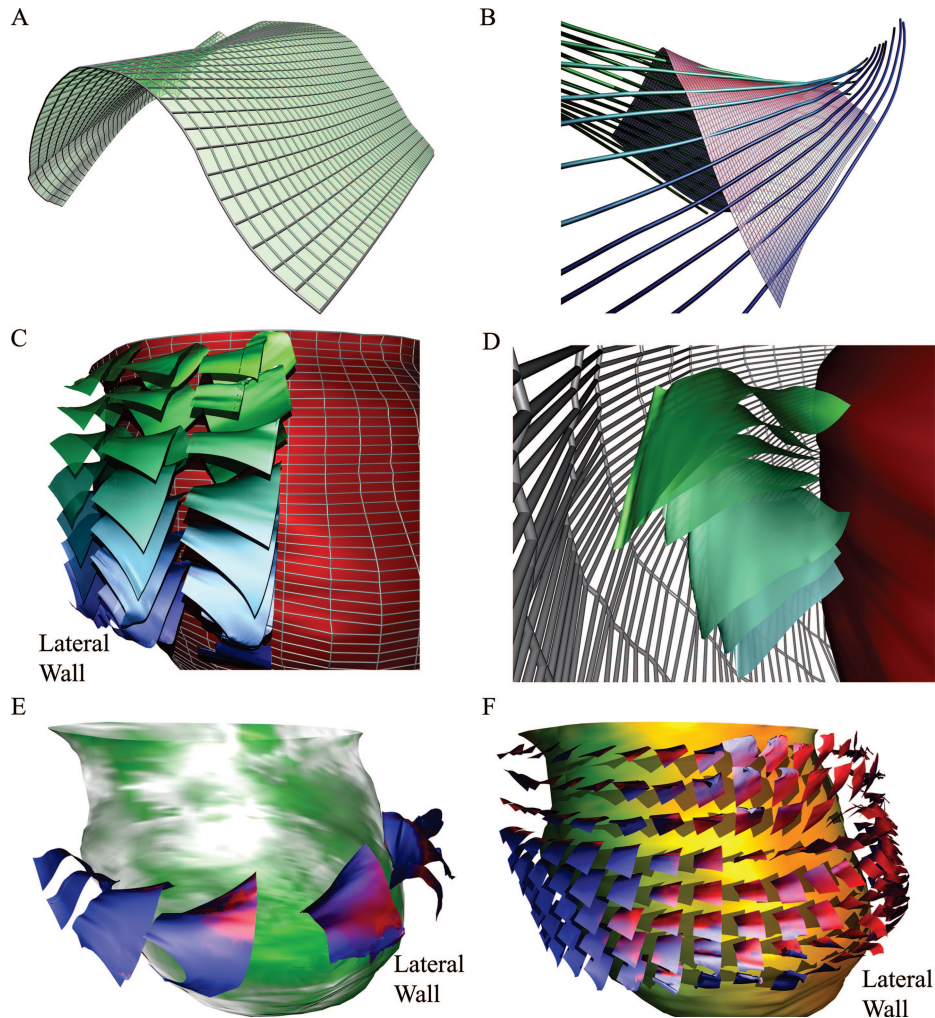


**FIGURE 6.** Visualization of the sheet structure of the left ventricle. A, One sheet reconstructed by our method. The line traveling left from the closest corner corresponds to the epicardium. The concave shape in the z coordinate along the long axis of the left ventricle is characteristic of a region close to the base of the LV. B, The fibers are shown embedded in the sheet surface. It can be noticed that the fibers lie completely on the surface. The color on the surface shows the third component of the fiber direction (red: small z component, blue: large z component). The surface twist clockwise with the fibers in the epicardial region, has a local maximum in the midwall where some circumferential fibers lie on it, and then goes down, twisting in the opposite direction with the fibers. C and D present sheets stacked crossing the ventricular wall. The twist of the sheets is noticeable with a concave curvature in the transverse section of the heart wall. The color of the sheet is only used to differentiate them. In (D), the endocardium corresponds to the red surface and the epicardium is shown by the mesh. E, Large sheets around the left ventricle positioned closer to the basal region. The color of the sheets encodes the z component of the fiber direction (blue: planar fiber, red: fiber going up or down). Some irregular structures can be seen close to the epicardium due to noise. The color of the endocardium encodes the z component of the sheet normal. The green color indicates a large z component (the sheet is almost in the radial plane); whereas the white transparent color indicates a more vertical direction (less planar sheets). F, Small sheet surfaces distributed over the entire left ventricle. The spatial variation shows a complex global structure. The color coding of the endocardium is the first and second component of the fiber direction and the color coding of the sheets is the same as in (E). In both panels (E) and (F), the lateral wall connects with the anterior wall on the left and the posterior wall on the right.

Our results were more similar to those reported by Geerts et al<sup>11</sup> in excised goat hearts except their range of angles were much larger than ours. Using DTMRI, they reported fiber angles ranging from  $-85^{\circ}$  to  $+50^{\circ}$ ,  $-75^{\circ}$  to  $+90^{\circ}$ ,  $-55^{\circ}$  to  $+85^{\circ}$ , and  $-40^{\circ}$  to  $+80^{\circ}$ , in the septal region, anterior region, intrapapillary muscle site (lateral region), and posterior region, respectively.

The histograms of the fiber angles show clearly distributions of negative angles for the epicardium and of positive angles for the endocardium. The histograms for the midwall show distributions about zero. The histograms for the endocardium show the greatest spread in the distributions and less so for the epicardium. This is another indication that the segmentation of the endocardial wall is

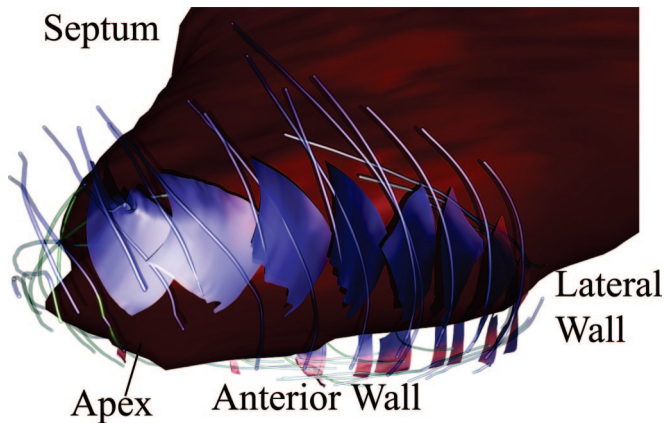


**FIGURE 7.** Reconstruction of the sheets in the apex. These sheets smoothly join the epicardium to the endocardium. The color of the surface encodes the third component of the fiber direction. In the region where the fiber angle is almost zero (red regions), the surface has very little twist and is almost planar. For the other case where the fibers have a larger  $z$  component, the curvature of the sheet is greater. The structures in the septal wall are not shown. This is because at this region the heart is linked with the right ventricle. The algorithm does not perform well due to the assumptions of how the surfaces cross the left ventricle that probably differ from surfaces embedded in the right ventricle. The orientation of the view is labeled on the figure.

more difficult due to papillary and trabecular muscle structures than segmentation of the epicardial wall.

A comparison of fiber tracking results from filtered and unfiltered data is presented in Figure 5. Fibers were tracked throughout the entire ventricle without filtering and after filtering. It can be noticed that the filtered data provide fibers that appear to be more parallel and the fiber bundles are easier to distinguish. The measurement of the angle  $\alpha$  is also plotted comparing the result for both cases. The plot shows that filtering does not impact the statistical average of the fiber angle in the midwall. However, small differences in value can be noticed in the epicardial regions.

The surfaces of the sheet structures for the midwall are presented in Figure 6 and for the apex in Figure 7. These surfaces were built starting with seed points positioned in the midwall and were grown in 4 orthogonal directions perpendicular to the normal of the surface (Fig. 2C). The variations of the sheet angle  $\beta$  through the wall and histograms of  $\beta$  for the regions in Figure 3A are also plotted in Figure 8. The sheet angle variation is not a strictly increasing or decreasing function of wall thickness as is the case for the fiber angle. The plots for the basal and apical regions show similarities for the anterior, lateral, and posterior walls but not so much for the septal wall. The histogram results show some similarity between regions, especially for the lateral wall. The epicardium, endocardium, and apex regions show more variation.

Our results from 1 human heart are difficult to compare with those of other investigations who obtained measurements from several hearts. Helm et al<sup>9</sup> reported several

observations from canine data that we need to investigate in more detail. We find as they that the majority of regions contained a dominant angle within the distribution of sheet angles. These findings are similar to histologic results reported by others,<sup>2,16,19,42</sup> indicating that there are dominant muscle layers. Also, our dominant populations seem to be located at  $50^\circ$  and  $100^\circ$ , which are close to but not exactly equal to  $45^\circ$  and  $117^\circ$  observed by Helm et al.<sup>9</sup> Histology measurements of Dokos et al<sup>3</sup> identified a dominant midwall muscle layer at  $\sim 45^\circ$  and another at  $\sim 135^\circ$  in pigs, and Ashikaga et al<sup>16</sup> observed angles at  $36^\circ$  and  $\sim 70\text{--}90^\circ$  apart in canines. Dominant angles have also been observed by Harrington et al<sup>19</sup> in hearts excised from sheep by directly measuring sheet angles of tissue sections cut transverse to the fibers. They identified 2 families of sheets with sheet angles of approximately  $-45^\circ$  and  $+45^\circ$ . These were angle measurements of the second eigenvector whereas our measurements of  $\beta$  were based on measurements of the third eigenvector. Therefore, their measurements would correspond to a  $\beta$  of  $+45^\circ$  and  $+135^\circ$ .

## DISCUSSION

A method is presented for generation of qualitative computer visualization of fiber and laminar structures in the normal human heart from ex vivo DTMRI data. In our implementation, the fibers are represented as shaded 3D tubes to improve the depth perception of the structure. The fiber angles are shown to vary smoothly across the wall from a negative (epi) to positive (endo) angle. Fibers lie within sheet surfaces (cleavage planes), but the knowledge of fiber directions is not sufficient to create visualization of the cleavage planes. This implies that the surfaces need parameterizations which are not related to the fiber directions. Our work helps demonstrate the relationships between fiber directions and laminar structure by providing high quality visualizations of both of these structures.

As it has been reported in the literature, the fiber angles are shown to vary smoothly as a linear function across the wall, but become more nonlinear near the endocardial and epicardial walls with significant increase in the gradients. Also, the variance of fiber directions is greater in these regions. This increase in noise may be due to both statistical effects of data acquisition and deterministic effects caused by the difficulty of segmenting the edges of the myocardium and, thus, potentially including papillary and trabecular muscle structures. This may be the reason for the actual minimum or maximum in the measured angle before the endocardial or epicardial boundary.

The process of fiber tracking is sensitive to noise. High frequency noise in the angles makes the fiber path irregular. Therefore, the path that follows a bundle of fibers might change from 1 bundle to another neighboring bundle. One could reduce this noise by averaging over more fibers; however, in our work, we depended upon the MLS regularization to provide the averaging. After the numerical solution of the differential equations [Eq. (1)], an anisotropic filtering with preferential weighting in the fiber direction was performed at every position to enable the reduction of data errors.

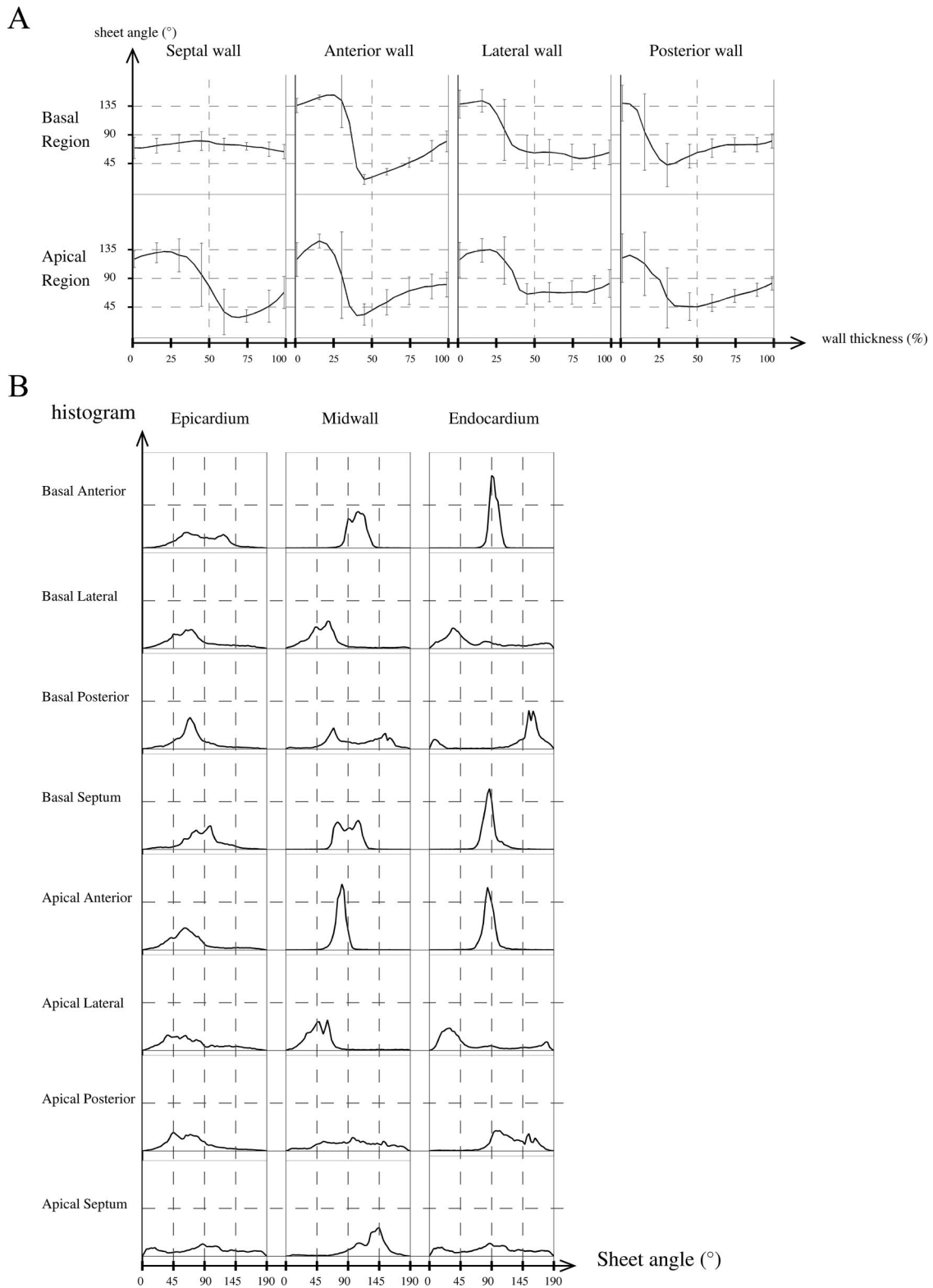


**FIGURE 8.** Quantitative distribution of the sheet angles  $\beta$ . **A**, Plot of the sheet angles from epicardium to endocardium in percent of the wall thickness for the regions as defined in Figure 4A. The values correspond to the average and standard deviation over 1800 nodes. **B**, Histograms of the sheet angles for epicardium, midwall, and endocardium sections of the regions as defined in Figure 4A.

In our work there were 2 possible sources of bias. One, the solution to the differential equations can introduce bias due to interpolation. Therefore, to minimize large errors in following the fiber over long distances, the Dormand-Prince Runge-Kutta method<sup>41</sup> with automatic error estimation was used. This method reduces the errors in the numerical solution of the differential equations. Two, we only had access to diffusion tensor data and did not have access to the original raw data used to reconstruct the diffusion tensor. In our algorithm it was necessary to interpolate the matrix components of the tensor field. However, there is a nonlinear transformation between a representation of the interpolation of the original data and the interpolation of the tensorial components. Therefore, a further improvement of our method, which needs to be investigated, may be to perform interpolation of the original data from which the tensor is calculated instead of interpolating the tensorial values.

The fiber directions were obtained based only on the largest eigenvectors of the diffusion tensors. The diffusion tensors in the heart have ratios of 1.46 and 1.74 between first and second and between the first and third eigenvalues, respectively. (Compare this with the brain which has a difference of a factor of 10 between the first and the second and third eigenvalues.) It was fairly easy to distinguish the first eigenvector from the other 2 eigenvectors. However, it was more difficult to determine the sheet structure which was obtained based on the second and third eigenvectors because they had magnitudes that were closer in value. Thus, a small amount of noise can easily invert the ordering of the second and third eigenvectors. Also, the 2 smallest eigenvectors have lower amplitudes than the first component and therefore the signal to noise is less. This is especially appreciated close to walls of the epicardium and endocardium where some surfaces of the cleavage planes appear to be noisy (Figs. 6C, E, F).

A better criterion to verify the correct interpretation of the 2 smallest eigenvectors may be needed to avoid misclassification by providing better a priori constraints on the orientation of the sheet normal. The current algorithm follows the radial direction and assumes that the structure of the sheet goes mainly across the wall. If this is not correct, the projected vector does not sufficiently control the directionality of the tracking and can lead to arbitrary directions for the sheet construction with amplitude that could approach zero. This problem appears specifically in the midwall of the anterior wall where the normal directions of the sheets are almost transverse to the wall. Also, if in some region the radial direction becomes perpendicular to the sheet, more a priori information may be needed to correctly visualize the sheet structure in this region. More robust methods may also be needed to enable the possibility of reconstructing surfaces in regions with interdigitating sheets oriented with a relative angle of about 70–90°. <sup>2,15,19</sup> The tensor model is unable to detect sheet crossings because the diffusion distribution at the crossing does not correspond to a Gaussian distribution. In this case a different model of diffusion would have to be taken into account.<sup>43</sup>

Because the precise structure of the sheet surfaces is not well known, it is difficult to conclude if fine structure of the surface is real or is due to noise. The sheet tracking algorithm was performed with the same regularization that was used for the fiber tracking. This constrained the tracked fibers to lie exactly inside the surface. However, another type of MLS regularization could also be implemented to filter more in the direction of the sheet than in the direction normal to the sheet.

Some other limitations are linked to the choice of POV-Ray software used for visualization. The visualization is done by ray tracing and because of that is very slow compared with other libraries such as OpenGL. Therefore, at the current stage of our development, interactive viewing of the results of the fiber and sheet tracking is not possible. More work is needed to make the visualization interactive.

Even with these difficulties, the structure and orientation of the sheets constructed in our work compares well with qualitative visualization of histologic measurements in transmural sections obtained from apex to base found in the literature.<sup>14</sup> At the epicardium it was difficult to obtain a smooth sheet surface because the difference between second and third eigenvalues for this region is smaller than for other regions of the myocardium. Thus, the variances associated with the directions of the second and third eigenvectors are increased in that region. This finding is consistent with Helm et al<sup>9</sup> who found no significant difference between second and third eigenvalues of the diffusion tensor in the epicardium. At the apex one observes a twist of the sheet around the apex (Fig. 7).

Several problems are encountered when using the current MRI technology to acquire in vivo human DTMR images of the human heart with the same high resolution and high signal to noise as that used in this article. The first is the long acquisition time. The data were acquired continuously for ~60 hours on a 1.5 T clinical scanner using a standard diffusion tensor acquisition protocol. This would be impossible for imaging the in vivo human heart. The signal noise is improved when going to higher field strengths.<sup>44–46</sup> However, there are several issues that need to be solved before high field DTMRI is feasible. The second problem is that the DTMRI approach which assumes a Gaussian diffusion model has difficulty tracking interdigitating sheets. This could possibly be solved by using q-space imaging<sup>47</sup> though this again would increase acquisition time. Q-space imaging has been applied to the spinal cord<sup>48</sup> and has also been applied ex vivo to study the complex fiber structure of the bovine tongue.<sup>48</sup> The third problem relates to performing any in vivo DTMRI of the moving heart. There is virtually only 1 group of researchers that have successfully accomplished this task.<sup>7,49–52</sup> The moving heart with its nonlinear deformation presents a significant challenge to performing in vivo DTMRI.

The technique presented here may have important implications for the in vivo study of heart structure in health and disease. For example, it may be useful for visualizing the reorganization of sheets over the cardiac cycle. Chen et al<sup>42</sup> showed using DTMRI in excised rat hearts that sheet reorientation within the subepicardial to subendocardial region is

a primary determinant of myocardial wall thickening. This information could be helpful in developing more advanced electromechanical models of the heart that are used in the study of the basic principles of cardiac function.

### ACKNOWLEDGMENTS

The authors acknowledge Drs. Patrick A. Helm and Raymond L. Winslow at the Center for Cardiovascular Bioinformatics and Modeling at Johns Hopkins University and Dr. Elliot McVeigh at the National Institutes of Health for providing the data that can be downloaded at [www.ccbm.jhu.edu](http://www.ccbm.jhu.edu). The authors would like to thank Dr. Mark Ratcliffe for helpful discussions. The authors also want to thank the reviewers for their helpful comments that went a long way to making it possible for us to present our technique to an audience with expertise in the field of myocardial structure.

### REFERENCES

1. Streeter DD Jr, Spotnitz HM, Patel DP, et al. Fiber orientation in the canine left ventricle during diastole and systole. *Circ Res*. 1969;24:339–347.
2. Costa KD, Takayama Y, McCulloch AD, et al. Lamellar fiber architecture and three-dimensional systolic mechanics in canine ventricular myocardium. *Am J Physiol*. 1999;276(2 pt 2):H595–H607.
3. Dokos S, Smaill BH, Young AA, et al. Shear properties of passive ventricular myocardium. *Am J Physiol Heart Circ Physiol*. 2002;283:H2650–H2659.
4. Humphrey JD. *Cardiovascular Solid Mechanics*. New York, NY: Springer; 2002.
5. Punske BB, Taccardi B, Steadman B, et al. Effect of fiber orientation on propagation: electrical mapping of genetically altered mouse hearts. *J Electrocardiol*. 2005;38(4 Suppl):40–44.
6. Fedak PW, Verma S, Weisel RD, et al. Cardiac remodeling and failure—From molecules to man (Part II). *Cardiovasc Pathol*. 2005;14:49–60.
7. Dou J, Tseng WY, Reese TG, et al. Combined diffusion and strain MRI reveals structure and function of human myocardial laminar sheets in vivo. *Magn Reson Med*. 2003;50:107–113.
8. Helm P, Beg MF, Miller MI, et al. Measuring and mapping cardiac fiber and laminar architecture using diffusion tensor MR imaging. *Ann N Y Acad Sci*. 2005;1047:296–307.
9. Helm PA, Tseng HJ, Younes L, et al. Ex vivo 3D diffusion tensor imaging and quantification of cardiac laminar structure. *Magn Reson Med*. 2005;54:850–859.
10. Tseng WY, Wedeen VJ, Reese TG, et al. Diffusion tensor MRI of myocardial fibers and sheets: correspondence with visible cut-face texture. *J Magn Reson Imaging*. 2003;17:31–42.
11. Geerts L, Bovendeerd P, Nicolay K, et al. Characterization of the normal cardiac myofiber field in goat measured with MR-diffusion tensor imaging. *Am J Physiol Heart Circ Physiol*. 2002;283:H139–H145.
12. Hunter PJ, Smaill BH, Nielsen PMF, et al. Mathematical model of the cardiac anatomy. In: *Computational Biology of the Heart*. New York, NY: John Wiley; 1996: Chap. 6.
13. Ohayon J, Chadwick RS. Effects of collagen microstructure on the mechanics of the left ventricle. *Biophys J*. 1988;54:1077–1088.
14. LeGrice IJ, Hunter PJ, Smaill BH. Lamellar structure of the heart: a mathematical model. *Am J Physiol*. 1997;272(5 Pt 2):H2466–H2476.
15. LeGrice IJ, Smaill BH, Chai LZ, et al. Lamellar structure of the heart: ventricular myocyte arrangement and connective tissue architecture in the dog. *Am J Physiol*. 1995;269(2 Pt 2):H571–H582.
16. Ashikaga H, Criscione JC, Omens JH, et al. Transmural left ventricular mechanics underlying torsional recoil during relaxation. *Am J Physiol Heart Circ Physiol*. 2004;286:H640–H647.
17. Arts T, Costa KD, Covell JW, et al. Relating myocardial laminar architecture to shear strain and muscle fiber orientation. *Am J Physiol Heart Circ Physiol*. 2001;280:H2222–H2229.
18. Robinson TF, Geraci MA, Sonnenblick EH, et al. Coiled perimysial fibers of papillary muscle in rat heart: morphology, distribution, and changes in configuration. *Circ Res*. 1988;63:577–592.
19. Harrington KB, Rodriguez F, Cheng A, et al. Direct measurement of transmural laminar architecture in the anterolateral wall of the ovine left ventricle: new implications for wall thickening mechanics. *Am J Physiol Heart Circ Physiol*. 2005;288:H1324–H1330.
20. Hsu EW, Muzikant AL, Matulevicius SA, et al. Magnetic resonance myocardial fiber-orientation mapping with direct histological correlation. *Am J Physiol*. 1998;274(5 Pt 2):H1627–H1634.
21. Scanlon PJ, Faxon DP, Audet AM, et al. ACC/AHA guidelines for coronary angiography. A report of the American College of Cardiology/American Heart Association Task Force on practice guidelines (Committee on Coronary Angiography). Developed in collaboration with the Society for Cardiac Angiography and Interventions. *J Am Coll Cardiol*. 1999;33:1756–1824.
22. Le Bihan D, Mangin JF, Poupon C, et al. Diffusion tensor imaging: concepts and applications. *J Magn Reson Imaging*. 2001;13:534–546.
23. Mori S, Barker PB. Diffusion magnetic resonance imaging: its principle and applications. *Anat Rec*. 1999;257:102–109.
24. Sitek A, Klein GJ, Gullberg GT, et al. Deformable model of the heart with fiber structure. *IEEE Trans Nucl Sci*. 2002;49:789–793.
25. Veress A, Segars W, Weiss JA, et al. Normal and pathological NCAT image and phantom data based on physiologically realistic left ventricle finite element models. *IEEE Trans Med Imaging*. 2006;25:1604–1616.
26. Mori S, van Zijl PCM. Fiber tracking: principles and strategies—a technical review. *NMR Biomed*. 2002;15:468–480.
27. Rohmer D, Sitek A, Gullberg GT. *Reconstruction and Visualization of Fiber and Sheet Structure with Regularized Tensor Diffusion MRI in the Human Heart*. Berkeley, CA: E.O. Lawrence Berkeley National Laboratory Report; 2006. LBNL-60277.
28. Helm PA, Younes L, Beg MF, et al. Evidence of structural remodeling in the dyssynchronous failing heart. *Circ Res*. 2006;98:125–132.
29. Pfeffer MA, Braunwald E. Ventricular remodeling after myocardial infarction. Experimental observations and clinical implications. *Circulation*. 1990;81:1161–1172.
30. Weber KT, Sun Y, Tyagi SC, et al. Collagen network of the myocardium: function, structural remodeling and regulatory mechanisms. *J Mol Cell Cardiol*. 1994;26:279–292.
31. Walker JC, Guccione JM, Jiang Y, et al. Helical myofiber orientation after myocardial infarction and left ventricular surgical restoration in sheep. *J Thorac Cardiovasc Surg*. 2005;129:382–390.
32. Beaulieu C. The basis of anisotropic water diffusion in the nervous system—a technical review. *NMR Biomed*. 2002;15:435–455.
33. Scollan DF, Holmes A, Winslow R, et al. Histological validation of myocardial microstructure obtained from diffusion tensor magnetic resonance imaging. *Am J Physiol*. 1998;275(6 Pt 2):H2308–H2318.
34. Zhukov L, Barr AH. Heart-muscle fiber reconstruction from diffusion tensor MRI. In: *IEEE Visualization Conference Proceedings*, Seattle, WA, October 19–24, 2003.
35. Ennis DB, Kindman G, Rodriguez I, et al. Visualization of tensor fields using superquadric glyphs. *Magn Reson Med*. 2005;53:169–176.
36. Peeters T, Vilanova A, Strijkers GJ, et al. Visualization of the fibrous structure of the heart. In: *Vision, Modeling, and Visualization*; November 22–24, 2006; Aachen, Germany, pp. 309–317.
37. Hunter PJ, Pullan AJ, Smaill BH. Modeling total heart function. *Annu Rev Biomed Eng*. 2003;5:147–177.
38. Zhukov L, Barr AH. Oriented tensor reconstruction: tracing neural pathways from diffusion tensor MRI. In: *IEEE Visualization Conference Proceedings*, Boston, MA, October 27–November 1, 2002.
39. Bassar PJ, Pajevic S, Pierpaoli C, et al. In vivo fiber tractography using DT-MRI data. *Magn Reson Med*. 2000;44:625–632.
40. Jones DK, Simmons A, Williams SC, et al. Non-invasive assessment of axonal fiber connectivity in the human brain via diffusion tensor MRI. *Magn Reson Med*. 1999;42:37–41.
41. Haier E, Norsett SP, Wanner G. *Solving Ordinary Differential Equations I, Nonstiff Problems*. Berlin, Germany: Springer; 2000.
42. Chen J, Liu W, Zhang H, et al. Regional ventricular wall thickening reflects changes in cardiac fiber and sheet structure during contraction: quantification with diffusion tensor MRI. *Am J Physiol Heart Circ Physiol*. 2005;289:H1898–H1907.
43. Ozarslan E, Mareci TH. Generalized diffusion tensor imaging and analytical

- relationships between diffusion tensor imaging and high angular resolution diffusion imaging. *Magn Reson Med.* 2003;50:955–965.
44. Fenchel M, Deshpande VS, Nael K, et al. Cardiac cine imaging at 3 Tesla: initial experience with a 32-element body-array coil. *Invest Radiol.* 2006;41:601–608.
  45. Michaely HJ, Nael K, Schoenberg SO, et al. Analysis of cardiac function—comparison between 1.5 Tesla and 3.0 Tesla cardiac cine magnetic resonance imaging: preliminary experience. *Invest Radiol.* 2006;41:133–140.
  46. Wintersperger BJ, Bauner K, Reeder SB, et al. Cardiac steady-state free precession CINE magnetic resonance imaging at 3.0 tesla: impact of parallel imaging acceleration on volumetric accuracy and signal parameters. *Invest Radiol.* 2006;41:141–147.
  47. Basser PJ. Relationships between diffusion tensor and q-space MRI. *Magn Reson Med.* 2002;47:392–397.
  48. Assaf Y, Mayk A, Cohen Y. Displacement imaging of spinal cord using q-space diffusion-weighted MRI. *Magn Reson Med.* 2000;44:713–722.
  49. Dou J, Reese TG, Tseng WY, et al. Cardiac diffusion MRI without motion effects. *Magn Reson Med.* 2002;48:105–114.
  50. Tseng WY, Reese TG, Weisskoff RM, et al. Myocardial fiber shortening in humans: initial results of MR imaging. *Radiology.* 2000;216:128–139.
  51. Tseng WY, Reese TG, Weisskoff RM, et al. Cardiac diffusion tensor MRI in vivo without strain correction. *Magn Reson Med.* 1999;42:393–403.
  52. Wu MT, Tseng WY, Su MY, et al. Diffusion tensor magnetic resonance imaging mapping the fiber architecture remodeling in human myocardium after infarction: correlation with viability and wall motion. *Circulation.* 2006;114:1036–1045.